



ELSEVIER

Available online at www.sciencedirect.com

SCIENCE @ DIRECT[®]

Journal of Magnetism and Magnetic Materials 285 (2005) 303–313

**Journal of
magnetism
and
magnetic
materials**

www.elsevier.com/locate/jmmm

Micromagnetic studies of cobalt microbars fabricated by nanoimprint lithography and electrodeposition

Darko Grujicic, Batric Pesic*

*Department of Materials Science and Engineering, College of Engineering, University of Idaho, McClure Hall, Moscow,
ID 83844-3024, USA*

Received 14 April 2004; received in revised form 29 July 2004
Available online 1 September 2004

Abstract

Micromagnetic and macromagnetic switching properties of cobalt bars with six different aspect ratios produced by electrodeposition of cobalt into patterns defined by nanoimprint lithography were studied. It was found that microbars in the demagnetized state formed configurations with closed magnetic flux. Magnetization along the long axis of the microbars resulted in a single-domain state of magnetization for microbars of all aspect ratios. In the remanent state, magnetization in microbars with smaller aspect ratios resumed the vortex configuration. Individual remanent curves, as well as the net remanent curve, were extracted from magnetic force microscopy images for microbars with all aspect ratios, and their agreement with the macroscopic magnetization measurements is discussed.

© 2004 Elsevier B.V. All rights reserved.

PACS: 75.50.Cc; 75.75.+a; 81.16.-c

Keywords: Electrodeposited cobalt; Magnetic microbar; Magnetic vortex; Magnetization reversal; Magnetic force microscopy; Vibrating sample magnetometry; Micromagnetic modeling

1. Introduction

Small ferromagnetic structures have received great attention in recent years because of their possible application in non-volatile magnetic random access memory (MRAM) elements [1], and

because they are well suited for studies of single domain magnetization reversal phenomena. Thin cobalt bars and ellipses [2–8], and circular dots [9–13], are among the common shapes that have been a subject of micromagnetic investigations. In studies of magnetization reversal in cobalt bars, the most common geometry used were the bars with square corners [2,4,6–8]. It was shown by micromagnetic modeling [14] that square corners of cobalt bars result in irreproducible switching

*Corresponding author. Tel.: +1-208-885-6569; fax: +1-208-885-2855

E-mail address: pesic@uidaho.edu (B. Pesic).

properties, and that an alternative shape has to be found in order to ensure the reproducible switching. Among various techniques for preparation of ferromagnetic elements, sputtering [2,10,13], evaporation [3,4,6,7,9] and molecular beam epitaxy [8], the electrochemical deposition has found limited application, mostly for production of elements with perpendicular magnetization [15–20].

This paper describes the results of micromagnetic (magnetic force microscopy—MFM) and macromagnetic (vibrating sample magnetometry—VSM) study of cobalt microbars with round corners, produced by nanoimprinting and electrodeposition. Among the parameters studied was the effect of aspect ratio of cobalt microbars, as well as the effect of edge roughness on the switching field range and the associated switching mechanisms. The results of micromagnetic simulations are also included.

2. Experimental

Silicon wafers (100) were cleaned in 12% HF acid, until the surface of the wafer showed no wetting. Cobalt microbars were then produced on cleaned silicon wafer substrates in the following steps: 80 nm thick copper film was evaporated onto Si (100) wafers using a Polaron 6100 evaporator. The wafers were then spin-coated with 495 K polymethylmethacrylate (PMMA). After softbake on a hot plate, PMMA was imprinted with a nickel DVD stamp in Obducat NanoImprinter v.2.5. The wafers were then subjected to reactive ion oxygen etching (RIE) in a Technics PE-IIA plasma etcher in order to remove a thin layer of PMMA in the imprinted voids and expose the underlying copper surface. Etching was followed by cobalt electrodeposition from a 0.05 M CoSO_4 solution, buffered with 0.5 M H_3BO_3 , at -1100 mV vs. Ag/AgCl reference electrode ($E_h^0 = +0.222 \text{ V}$) for 10 s using a CH Instruments 760b potentiostat/galvanostat. No magnetic fields were applied to the substrate during electrodeposition. After electrodeposition, the remaining PMMA was removed by ashing in oxygen plasma, followed by final cleaning in a hot photoresist

remover solution (MicroChem). The flowsheet of the processing steps involved, and an atomic force microscopy (AFM) height image of the final product, electrodeposited cobalt microbars, are presented in Fig. 1.

The magnetic properties of the cobalt microbars were investigated on a macroscale by vibrating sample magnetometry (ADE DMS model 886) and on a microscale by magnetic force microscopy (VEECO DI Nanoscope IIIa, MultiMode, frequency modulation, regular cobalt–chromium coated MFM tips).

DVD stamp was chosen for patterning because the DVD tracks consist of microbars with rounded corners and well-defined aspect ratios. Deposited features were categorized in six classes according to the length-to-width aspect ratio (AR) as follows: 1.43; 2.14; 2.86, 3.57; 4.26; and 5.00. The width of all the microbars was 700 nm, and their height was 35 nm. The separation between the

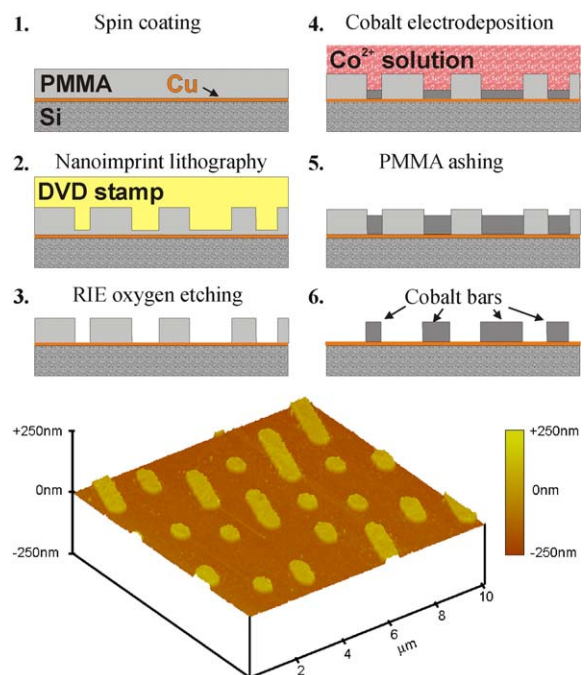


Fig. 1. Flowsheet of the processing steps used for electrodeposition of cobalt microbars. The bottom picture is an AFM image of resulting cobalt microbars (10 × 10 μm , 3D height mode).

individual microbars was at least 1000 nm in all directions.

3. Results and discussion

3.1. Crystallographic structure of deposited cobalt

The crystallographic phase of deposited cobalt microbars is important for magnetic studies [21], due to different magnetocrystalline anisotropies of different crystallographic phases. Stable crystallographic phase of bulk cobalt at room temperature is hexagonal closely packed (HCP) with uniaxial magnetocrystalline anisotropy. In contrast, thin cobalt films deposited on copper substrates grow with pseudomorphic face centered cubic (FCC) structure because of small crystallographic misfit between the FCC copper and cobalt [21,22]. Deposited FCC cobalt has cubic magnetocrystalline anisotropy with $\langle 111 \rangle$ easy direction [21] similar to that of FCC nickel. Both magnetocrystalline anisotropy and magnetoelastic anisotropies (emanating from the strain at the Cu/Co interface) of FCC cobalt are smaller than those of HCP cobalt [23]. In order to determine the crystallographic structure of cobalt electrodeposited in this study, continuous cobalt film was electrodeposited under the same conditions as cobalt microbars and examined by X-ray diffraction measurement. The X-ray spectrum of a bare copper substrate evaporated onto Si (100) exhibited a strong peak associated with FCC (002) reflection and a small peak associated with FCC (111) reflection, indicating a strong {002} texture. The strong {002} copper texture is a result of epitaxial growth on (100) silicon surface [22]. Same reflections were observed from the sample with deposited cobalt film, indicating FCC cobalt structure with {002} texture, pseudomorphically grown along $\langle 001 \rangle$ direction. No peaks associated with HCP cobalt reflections were observed. Due to {002} texture of deposited cobalt, the easy $\langle 111 \rangle$ directions of each crystallite will be inclined 35.2° from (100) plane. Because the cobalt film is textured, easy axes are pointing in random directions, so there should be no magnetocrystalline anisotropy in plane of the microbars.

3.2. Magnetic configurations of cobalt microbars in demagnetized state

Cobalt microbars were imaged in demagnetized state using magnetic force microscopy after AC demagnetization. AC demagnetization was performed with the sample placed in VSM in such way that the long axis of the bars was parallel to the applied external magnetic field. The amplitude of oscillating demagnetization field decreased successively by 10% in every half-cycle from the initial field of 5 kOe until the final field of 1 Oe was reached. Each line of the image was produced by first scanning the sample in intermittent contact mode to image the sample topography, and then in the lift mode with the tip lifted 100 nm off the surface, where the frequency of the tip was affected only by the magnetic interactions between the tip and the sample. Several characteristic magnetic configurations of cobalt microbars, observed in the demagnetized state, are presented in Fig. 2.

Simulated magnetization states presented in Fig. 2a–d in the middle and bottom rows were calculated by using the “Object Oriented Micro-Magnetic Framework”—OOMMF code in public domain, which performs time integration of the Landau–Lifshitz–Gilbert equation [24]. The images represent the magnetic pole density distributions at the surface of the microbars, calculated from the divergence component of the

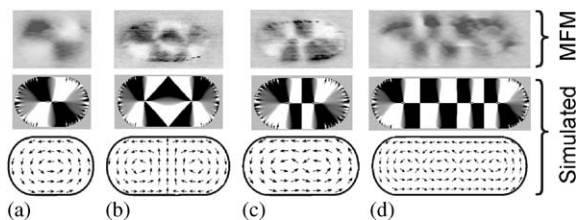


Fig. 2. Top row—MFM frequency modulation images of cobalt microbars in demagnetized state, taken at 100 nm lift height; middle row—simulated MFM images representing pole density distributions, and bottom row—direction of magnetization vectors corresponding to the simulated configurations in the middle row. The observed configurations are: (a) four-domain (or “vortex”) state in AR 1.43 microbar; (b) seven-domain (or “diamond”) state in AR 2.14 microbar; (c) cross-tie state in AR 2.14 microbar; and (d) cross-tie state in AR 3.57 microbar. Vertical scale for the MFM images is 5 Hz, and for simulated MFM images is 3000 A m⁻¹ (37.7 Oe).

magnetization perpendicular to the microbars (1) [25]

$$\rho = \nabla \cdot \mathbf{H} = -\nabla \cdot \mathbf{M} \quad (1)$$

where ρ is pole density, \mathbf{H} is the magnetic field vector, and \mathbf{M} is the magnetization vector. Saturation magnetization used for modeling was that of HCP cobalt, $M_s = 1.4 \times 10^6 \text{ A m}^{-1}$, since saturation magnetization of FCC and HCP cobalt are identical [21,26]. The cell size used for modeling was $10 \text{ nm} \times 10 \text{ nm} \times$ film thickness (35 nm), and the K_1 coefficient of the magnetocrystalline anisotropy was set to zero, simulating polycrystalline cobalt microbars. The exchange stiffness parameter A was initially set to $1.4 \times 10^{-11} \text{ J m}^{-1}$. Damping coefficient α was set to the default value of 0.5, although damping factor was not important since all of the magnetization configurations in Fig. 2a–d were simulated in the remanent state. Simulations were stopped when the residual torque fulfilled the condition:

$$|\vec{m} \times \vec{H}| < 10^{-6}.$$

First two configurations, vortex, (Fig. 2a) and diamond, (b) were obtained by total energy minimization from the initial random magnetization state. Resulting vortex and diamond states have already been shown to exist in demagnetized cobalt [7,8,12] and permalloy [27–30] elements. The third type of magnetization—cross-tie type, as given in Fig. 2c and d, could not be obtained by energy minimization from the initially random magnetization state. In order to simulate the cross-tie magnetization state, it was postulated that during the AC demagnetization, a trans-axial 180° Neel type wall forms along the axis parallel to the external field, when the amplitude of the AC magnetic field oscillations becomes lower than the individual coercivity of a particular microbar. When the initial magnetization configuration was set to include a trans-axial 180° Neel wall, it was found that the resulting simulated remanent states did have checkerboard configurations, like the ones in Fig. 2c and d. The number of checkerboard fields in the simulated MFM image, however, was highly sensitive on the value of exchange stiffness constant A . Only with A set to $2.2 \times 10^{-11} \text{ J m}^{-1}$ it was possible to match the number of checkerboard

fields in both MFM images, Fig. 2c and d. Setting the exchange stiffness value below $2.2 \times 10^{-11} \text{ J m}^{-1}$ resulted in the larger number of checkerboard fields, while with exchange stiffness higher than $2.2 \times 10^{-11} \text{ J m}^{-1}$ the number of checkerboard fields decreased below that in the MFM images. The abrupt bright-to-dark contrast change in the real and simulated MFM images comes from the abrupt change of magnetization direction along 45° Neel walls that originate from the vortex cores in the cross-ties, as previously observed in cross-tie walls of continuous thin cobalt films [31]. Magnetization configuration similar to the one in Fig. 2c and d was observed in long permalloy bars magnetized along the short axis ([32] Fig. 4b, middle image), but the reference [32] does not provide the explanation on the magnetization configuration of the elements.

3.3. Effect of aspect ratio on switching field distribution—MFM remanent magnetization curves

The study focused next on how the aspect ratio of the microbars affects the switching of their magnetization direction. In order to determine the effect of the extent of shape anisotropy on the switching properties of cobalt microbars, remanent curves were extracted from the MFM images. From the VSM measurements of the sample magnetization along the long axis of the microbars, it was found that the saturation magnetization was achieved at $\pm 600 \text{ Oe}$. The sample was subsequently saturated at $+600 \text{ Oe}$; the field reversed to a certain negative value, and afterward shut off. The sample was then transferred to MFM for characterization in the remanent state. Each MFM image included about 350 microbars of the various aspect ratios listed above. Microbars with a linear single-domain state in the direction of the saturation field were assigned a value of +1, while the ones with a linear single-domain state in the direction antiparallel to the direction of the saturation field (parallel to the direction of the reverse field) were assigned a value of -1. Microbars with a low magnetic contrast in MFM images were assigned a value of zero. The low magnetic contrast of some of the microbars resulted from the magnetic flux closure within

the microbars, achieved either through a vortex or through a multi-domain configuration, similar to those in Fig. 2a–d. These microbars are collectively referred to as “demagnetized” microbars.

Numerous microbars of all aspect ratios that appeared in each MFM image enabled statistical interpretation of the results of magnetization study in remanent state. For specific aspect ratio, remanent magnetization curves in Fig. 3a–f were constructed by subtracting the number of microbars with negative magnetization from the number of microbars with positive magnetization, and dividing the result by the total number of microbars with the involving aspect ratio. In order to estimate the extent of dipolar coupling between microbars in the remanent state, dipole field emanating from a AR 5.00 bar and acting at a distance of 1 μm along the long axis was calculated. This case represented the highest possible magnetic field found in the sample at the remanence. The field was calculated according to expression (2) [33]:

$$H = \frac{2prl}{\left(r^2 - \frac{l^2}{4}\right)^2}, \quad (2)$$

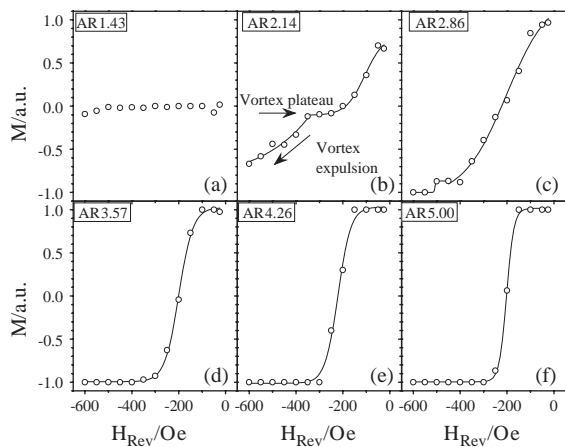


Fig. 3. Remanent curves of cobalt microbars extracted from MFM images for microbars with the following length-to-width aspect ratios: (a) 1.43, (b) 2.14, (c) 2.86, (d) 3.57, (e) 4.26, and (f) 5.00. Open circle symbols are experimental data, lines are Boltzmann-type sigmoidal curve fits. Note that the microbars with two smallest aspect ratios were not saturated. For microbars with higher aspect ratio, the width of the switching field range decreased with the increase of aspect ratio.

where p is the pole strength ($= Mhw$); M the saturation magnetization (emu cm^{-3}); l , h and w the length, height and width of the microbar (cm); and r the distance from the center of the microbar to a point in which the field is calculated (cm). Calculated field has magnitude of 33 Oe, which is lower than the observed coercivity of microbars (~ 200 Oe), so the effect of dipolar coupling should be negligible.

From Fig. 3a, it follows that the configuration of magnetic domains for microbars with the smallest aspect ratio was unaffected by the reversal field. MFM images show that their stable remanence state was a vortex state. Microbars with AR 2.14 became demagnetized at about -200 Oe, Fig. 3b). Between -200 Oe and -350 Oe, the remanent magnetization curve formed a plateau at zero magnetization, followed by an increase of magnetization beyond -350 Oe. A zero magnetization plateau resulting from trapped magnetization vortices has also been observed by others [27]. A step between -350 Oe and -400 Oe corresponds to the initiation of vortex expulsion [27,34] and magnetization along the direction of the applied field. The stability of the vortex magnetization in the remanent state for AR 2.14 microbars is evident, since at -600 Oe the total magnetization was -0.7, indicating that 70% of the microbars were in a single domain state.

Microbars with aspect ratios higher than 2.14, Fig. 3c–f underwent a complete reversal of magnetization direction in the range of reversal fields investigated, as indicated by the change of magnetization from +1 to -1. The width of the switching field distribution was evidently dependent on the aspect ratio of the microbars. In order to estimate the width of the switching field range, remanent magnetization data in Fig. 3b–f were fitted with Boltzman-type sigmoidal curves. The data in Fig. 3b was fitted with two sigmoidal curves, first in the range -25 – -350 Oe, and second in the range -350 – -600 Oe. Similarly, the data in Fig. 3c was fitted first in the range -25 – -450 Oe and then in the range -450 – -600 Oe. The curves were then differentiated with respect to the magnetic field and fitted with a Gaussian distribution. Two standard deviations (2σ) of the switching field distribution were then determined

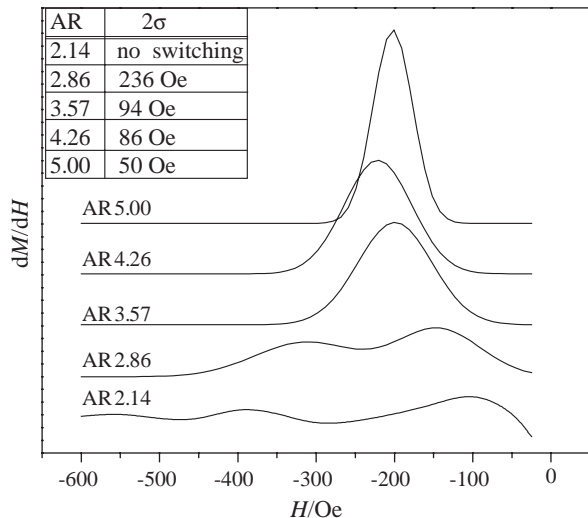


Fig. 4. dM/dH of curves in Fig. 3b–f as a function of reversal field. Note the existence of two peaks for the curves representing AR 2.14 and 2.86 microbars.

as full-width at half-maximum (FWHM) of the peak on the dM/dH curve, Fig. 4. The width of the switching field distribution for microbars with AR 2.86, 3.57, 4.26 and 5.00, determined from dM/dH curves, was 236, 94, 86 and 50 Oe, respectively. In these ranges, 95% of the microbars with a specific aspect ratio will flip their magnetization orientation. The peaks on dM/dH curves for AR 3.57, 4.26 and 5.00 were all centered around -200 Oe, the nominal switching field, which was also the coercive field of the entire sample.

From Fig. 4, it can also be seen that dM/dH curve for AR 2.14 microbars shows two peaks. The peak on the right corresponds to the formation of vortices, while the peak on the left corresponds to their disappearance [27]. Two peaks were also observed in the dM/dH curve for AR 2.86 microbars, indicating transition through a vortex state. However, in AR 2.86 microbars the peaks are closer together than for AR 2.14 microbars, indicating an earlier expulsion of vortices.

3.4. Switching mechanisms

In order to determine the mechanisms of magnetization switching in cobalt microbars, the

model of coherent spin rotation—the Stoner–Wohlfarth model [35] was applied first. By regarding cobalt microbars as single-domain magnetic dipoles, and assuming that the reversal of magnetization direction occurs through coherent rotation of spins, different coercivities of microbars with different aspect ratios stemming from their different shape anisotropies can be calculated by approximating the microbars with general ellipsoids with known demagnetizing factors [36]. By substituting the calculated demagnetization coefficients into the appropriate expression for the coercivity of particles reversing their magnetization by coherent in-plane rotation, (3) [33]

$$H_{ci} = (N_a - N_b)M_s, \quad (3)$$

where H_{ci} the coercive field, N_a and N_b demagnetization factors along the short and long axis, and M_s the saturation magnetization of cobalt (1422 emu cm^{-3}), calculated coercivities for microbars with different aspect ratios were between -80 Oe for AR 1.43 microbar and -750 Oe for AR 5.00 microbar. Since observed coercivities for microbars with AR 2.14 and above were all at about -200 Oe, which was also the coercivity of the entire sample, it follows that the reversal of magnetization directions in cobalt microbars does not take place through coherent spin rotation. Incoherent magnetization reversal should also be expected from a large difference in the dimensions of the microbars compared to the exchange length of cobalt (3.37 nm).

Next, the OOMMF code [24] was used to simulate the remanent magnetization curve in a single AR 5.00 cobalt microbar. Magnetic field was swept parallel to the long axis of the bar from +1000 to -1000 Oe, with a small magnetic field component applied along the short axis in order to break the symmetry, so that the resulting external magnetic field vector was rotated 2° from the long axis. An actual AFM image of AR 5.00 microbar was used as a template for the simulation. AFM image of the cobalt microbar shows edge roughness and imperfections along the sides of the microbar. In simulating the AFM image of AR 5.00 microbar, the AFM-tip—microbar-edge convolution, which may be responsible for different

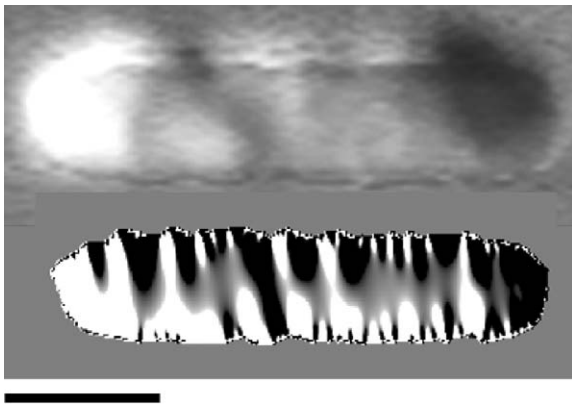


Fig. 5. Top—MFM frequency modulation image of AR 5.00 microbar in a remanent, single domain state after saturation to +1000 Oe; Bottom—simulated MFM image of the same microbar. Scale bar is 1 μm . MFM image of magnetic field divergence component was obtained by simulation that included two steps: applied field of 1000 Oe along the long axis and 35 Oe along the short axis, followed by the applied field of 0 Oe along both axes.

roughness of the edges in the image compared to the actual roughness, was not taken into account. The resolution of the image was sufficiently high, so that one 10×10 nm cell used in simulation corresponded roughly to an area of 5×5 pixels in the image. According to the simulation, there is a relatively good correlation between the simulated and the actual MFM image of the same microbar, Fig. 5 in the remanent state after magnetization to +1000 Oe.

From Fig. 5, it follows that the uneven edges of microbar result in formation of edge domains, which are manifested as additional contrast in the MFM image. Formation of edge domains due to edge roughness was also predicted theoretically [37].

Remanent magnetization curve calculated by micromagnetic simulation using the microbar given in Fig. 5 as a template is compared in Fig. 6 to the remanent magnetization curve for AR 5.00 microbars from Fig. 3f.

According to Fig. 6, there is a relatively good agreement between the simulated remanent magnetization curve and the MFM remanent magnetization curve from -25 Oe up to -250 Oe. The coercivity of the simulated remanent magnetiza-

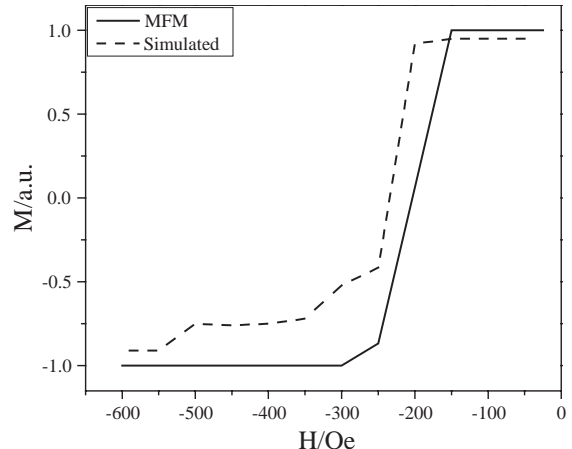


Fig. 6. Remanent magnetization curve for AR 5.00 microbar from Fig. 3f (solid line), compared to the simulated remanent magnetization curve in the range from -25 Oe to -600 Oe.

tion curve is about 30 Oe higher than of that determined by MFM. Simulated remanent magnetization curve for reversal fields higher than -250 Oe deviates from the one determined by the MFM. The deviation is caused by the remaining vortex cores at the edges of the microbar in the simulation, a state that was not observed in the MFM images. According to the simulation, magnetization reversal takes place through formation of theoretically predicted [38] vortex and transverse head-to-head domain walls. Cores of magnetization vortices nucleate first at the oblique ends of the microbars. Reduced coercivity due to formation of domain wall traps at the rough edges is consistent with theoretical calculations [37]. This conclusion can be extended to all other microbars with AR 2.14 – 5.00, because their calculated coercivities for coherent spin rotation mechanism were all higher than -200 Oe. It therefore follows that magnetization reversal in all microbars takes place by vortex nucleation, regardless of their aspect ratio. The width of the switching field then only depends on the stability of vortex states in microbars of particular aspect ratio. Because stability of vortex states decreases with increasing aspect ratio, the width of the switching field distribution decreases with the increasing aspect ratio as well. In addition, for the thickness of 35 nm, existence of vortex domain walls is

energetically more favorable than of the transverse walls [38].

The validity of the remanent curves constructed from MFM images in Fig. 3a–f was also tested by the actual measurements of sample remanence by a bulk measurement method; e.g., VSM measurements. Remanent magnetization of the sample was measured by VSM under the same conditions as those under which the sample was prepared for MFM imaging: by saturating it to +600 Oe, reversing the field to a certain value between −25 and −600 Oe, and then measuring the remanent magnetization. The measured remanent magnetization is presented in Fig. 7. The remanent magnetization curve of the entire sample in Fig. 7 was constructed by subtracting the total number of bars with negative magnetization from the total number of bars with positive magnetization, and dividing the result by the total number of bars within the MFM image.

There is strikingly good agreement between the VSM and MFM remanent magnetization curves in Fig. 7. The deviation of the remanent magnetization curves from the magnetization curve beyond

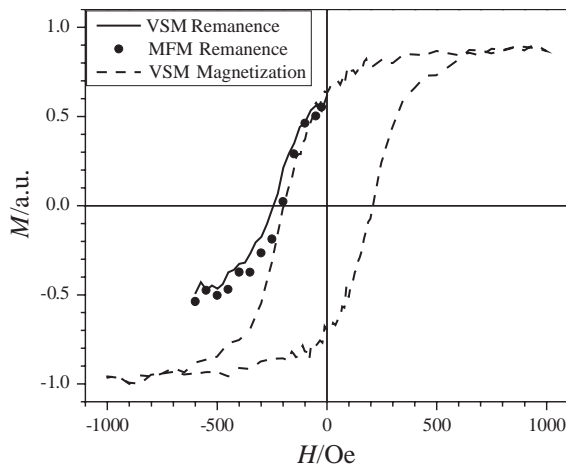


Fig. 7. The net MFM remanent magnetization curve (solid circles) compared to the VSM remanent magnetization curve (solid line) and the VSM magnetization curve (dashed line). The VSM magnetization curve was obtained by measuring magnetization while sweeping the field in the (+1000, −1000) Oe range. The MFM curve was normalized with respect to the total number of cobalt microbars in one image, while VSM curves were normalized with respect to the saturation magnetization determined from the VSM magnetization curve.

−300 Oe confirms that some of the microbars with a single-domain magnetization state resumed the demagnetized state upon the removal of the externally applied magnetic field. Finally, the good agreement between the MFM and VSM remanent magnetization curves validates the method of constructing individual remanent magnetization curves as a function of the aspect ratio in Fig. 3a–f, by using the MFM images.

3.5. Effect of aspect ratio on stability of vortex states

Another parameter of interest was the remanent magnetization state of microbars after the field reversal to the coercive field of −200 Oe. The mechanism of magnetization reversal is important for the design of MRAM elements. In ring- or disc-shaped MRAM elements that utilize different directions of vortex magnetization, single-domain states are undesirable. On the other hand, in MRAM elements that utilize magnetization orientations of single domains, the appearance of stable vortex states leads to irreproducible switching, and therefore a vortex-free stable magnetization states are required. Remanent magnetization states of microbars as a function of their aspect ratio after the field reversal to the coercive field of −200 Oe were thus indicative of the stability of the vortex states. The fraction of demagnetized microbars in the remanent state as a function of their aspect ratio is presented in Fig. 8. The graph in Fig. 8 was constructed by counting the number of demagnetized microbars in the MFM image taken in the remanent state after the field reversal to −200 Oe, and then dividing that number by the total number of microbars of the particular aspect ratio counted in the same image.

Zero total magnetization of cobalt microbars with the same aspect ratio could be a result of: (a) microbars assuming the vortex or multi-domain magnetization states (Fig. 8, upper schematics), or (b) having an equal number of single-domain microbars with antiparallel orientations, whose magnetizations cancel out (Fig. 8, lower schematics). From Fig. 8, it follows that the microbars with the lowest aspect ratio were 100% in a demagnetized state at the remanence. The fraction

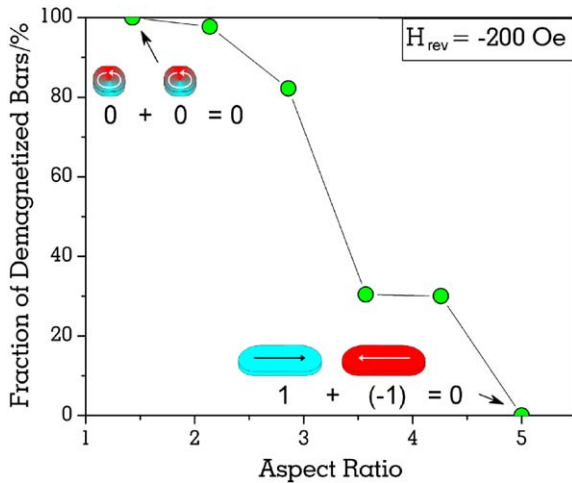


Fig. 8. Fraction of demagnetized microbars (microbars with either a vortex or multi-domain magnetization states) at the remanence, after magnetization to +600 Oe and reversal to -200 Oe, as a function of aspect ratio, as determined by MFM. Schematic representations show how a zero net magnetization is achieved in the two extreme cases.

of microbars demagnetized at -200 Oe decreased with the increasing aspect ratio, and finally became zero for the microbars with the aspect ratio 5.00. The decreasing fraction of demagnetized microbars with increasing aspect ratio indicates that stability of vortex states decreases with the increasing aspect ratio, due to the increase in shape anisotropy.

3.6. Sample – MFM tip interaction

During the MFM imaging, it was observed that the magnetization states of some of the AR 2.14 microbars could be affected by the magnetic field of the MFM tip. An example is given in MFM image in Fig. 9. The image was taken after saturating the sample at +600 Oe, reversing the field to -500 Oe and then imaging at the remanence.

It was found that about half of the AR 2.14 microbars in Fig. 9 were in a single-domain state, while the other half were in a “demagnetized” state, and were not visible in the image due to their weak magnetic contrast. During the imaging, several AR 2.14 bars with a strong single-domain

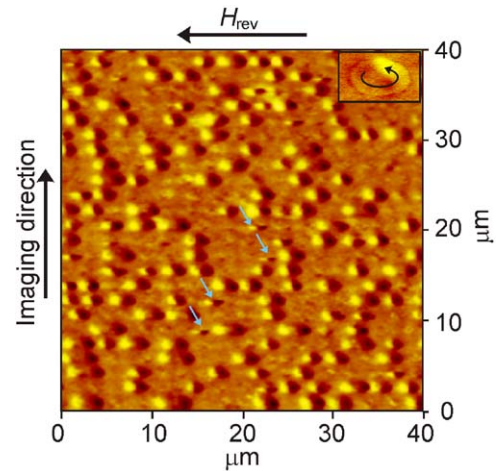


Fig. 9. $40 \times 40 \mu\text{m}$ MFM image taken at remanence after saturating the sample to $H_{\text{sat.}} = +600$ Oe and then reversing the field to $H_{\text{rev.}} = -500$ Oe. The arrows in the image are pointing at some of the AR 2.14 microbars whose magnetization had changed from a single-domain to a demagnetized state during imaging (several other AR 2.14 microbars that switched during imaging can also be found in the image). The inset shows an MFM image of a AR 2.14 microbar in a vortex magnetization state. Lift height was 100 nm.

type contrast disappeared from the image while the tip was in their immediate proximity. The arrows in Fig. 9 mark a few such microbars. A transition from a single-domain to a demagnetized state in AR 2.14 microbars was induced by the MFM tip during imaging, as witnessed in Fig. 9. The same figure includes an MFM image of AR 2.14 microbar in a demagnetized vortex state. The frequency range used for the image in the inset was 5 Hz, instead of the 10 Hz used for the large image, to better highlight the vortex state of the microbar. The influence of the MFM tip on magnetization state in nanosized discs has also been observed by other research groups (see Fig. 15.9 in Ref. [39]). Microbars with higher aspect ratios, AR 2.86 to 5.00, were all in a single-domain state and were not affected by the magnetic field of the MFM tip. The effect of MFM tip field on the magnetization of the microbars can be estimated by calculating the tip field strength at the distance of 100 nm (lift height used for MFM imaging). Using the cylindrical model of the tip [40], and saturation magnetization of 870 emu cm^{-3} for CoCr MFM

tips [41], calculated tip field was ~ 16 Oe. This field is too low to induce the change of magnetization configuration in the sample. However, since the CoCr MFM tip coating is magnetically harder than studied microbars (coercivity ~ 360 Oe [41,42]), and the field at the tip surface determined by electron holography is 620 Oe [43], which is higher than the saturation magnetization of microbars in the plane, it is possible that the micromagnetic configurations were affected by the MFM tip while performing intermittent contact mode scans. Magnetic field of the tip, perpendicular to the sample surface, could initiate vortex formation. Microbars with small AR in which vortex configurations are energetically more stable would be affected by the tip field, while the ones with larger AR in which vortex configurations are unstable would not be affected, which coincides with the observed effect in Fig. 9.

4. Conclusion

In conclusion,

1. The usefulness of application of nanoimprint lithography and electrodeposition for fabrication of metal microbars, cobalt in this study, of various length-to-width aspect ratios was demonstrated.

2. Cobalt microbars in AC demagnetized states had vortex, diamond or cross-tie magnetic configurations, whose origins were correlated to different initial magnetization states through micromagnetic modeling. By micromagnetic modeling of the MFM images showing cross-tie magnetization, the value of exchange stiffness constant $A = 2.2 \times 10^{-11} \text{ J m}^{-1}$ was determined.

3. In externally applied field, magnetization configurations changed to a single-domain state.

4. The correlation between the width of switching field range to the shape anisotropy, defined according to length-to-width aspect ratio, was established.

5. Micromagnetic modeling revealed that magnetization reversal takes place through vortex generation at the edge domains, which reduces the coercivity of the microbars, compared to the calculated coercivities for coherent spin rotation mechanism.

6. There is an excellent agreement between the remanent magnetization curves obtained by micromagnetic analysis (MFM) and macromagnetic characterization (VSM).

Acknowledgements

This work was sponsored by the US Department of Defense, Department of the Navy, Office of Naval Research, Grant Number N000140110829, and The National Science Foundation RII Award (EPS 0132626). Help by Obducat (Malmo, Sweden) during acquisition of nanoimprint equipment and technical training is greatly appreciated.

References

- [1] G.A. Prinz, Science 282 (1998) 1660.
- [2] R.D. Gomez, M.C. Shih, R.M.H. New, R.F.W. Pease, R.L. White, J. Appl. Phys. 80 (1) (1996) 342.
- [3] L. Kong, S.Y. Choy, J. Appl. Phys. 80 (9) (1996) 5205.
- [4] Y.Q. Jia, S.Y. Choy, J.G. Zhy, J. Appl. Phys. 81 (8) (1997) 5461.
- [5] J.A. Johnson, M. Grimsditch, V. Metlushko, P. Vavassori, B. Ilic, P. Neuzil, R. Kumar, Appl. Phys. Lett. 77 (26) (2000) 4410.
- [6] Y. Hao, F.J. Castano, C.A. Ross, B. Vogeli, M.E. Walsh, H.I. Smith, J. Appl. Phys. 91 (10) (2002) 7989.
- [7] W.C. Uhlig, H. Li, B.S. Han, J. Shi, J. Appl. Phys. 91 (10) (2002) 6943.
- [8] J. Bekaert, M.J. Van Bael, D. Buntinx, K. Temst, C. Van Haesendonck, V.V. Moshchalkov, L. Lagae, J. De Boeck, G. Borghs, Rev. Sci. Inst. 74 (6) (2003) 3062.
- [9] J. Raabe, R. Pulwey, R. Sattler, T. Schweinbock, J. Zweck, D. Weiss, J. Appl. Phys. 88 (7) (2000) 4437.
- [10] A. Lebib, S.P. Li, M. Natali, Y. Chen, J. Appl. Phys. 89 (7) (2001) 3892.
- [11] M. Natali, A. Lebib, E. Cambril, Y. Chen, I.L. Prejbeanu, K. Ounadjela, J. Vac. Sci. Technol. B 19 (6) (2001) 2779.
- [12] I.L. Prejbeanu, M. Natali, L.D. Buda, U. Ebels, A. Lebib, Y. Chen, K. Ounadjela, J. Appl. Phys. 91 (10) (2002) 7343.
- [13] M. Natali, A. Lebib, Y. Chen, I.L. Prejbeanu, K. Ounadjela, J. Appl. Phys. 91 (10) (2002) 7041.
- [14] Y. Zheng, J.G. Zhu, J. Appl. Phys. 81 (8) (1997) 5471.
- [15] W. Xu, J. Wong, C.C. Cheng, R. Johanson, A. Scherer, J. Vac. Sci. Technol. B. 13 (6) (1995) 2372.
- [16] S.P. Li, A. Lebib, Y. Chen, Y. Fu, M.E. Welland, J. Appl. Phys. 91 (12) (2002) 9964.
- [17] C.A. Ross, M. Hwang, M. Shima, J.Y. Cheng, M. Farhoud, T.A. Savas, H.I. Smith, W. Schwarzacher,

- F.M. Ross, M. Redjdal, F.B. Humphrey, Phys. Rev. B 65 (2002) 144417.
- [18] A. Robinson, W. Schwarzacher, J. Appl. Phys. 93 (10) (2003) 7250.
- [19] M. Vazquez, K. Pirota, M. Hernandez-Velez, V.M. Prida, D. Navas, R. Sanz, F. Batallan, J. Velazquez, J. Appl. Phys. 95 (11) (2004) 6642.
- [20] I. Zana, G. Zangari, J. Appl. Phys. 91 (10) (2002) 7320.
- [21] T. Suzuki, D. Weller, C.-A. Chang, R. Savoy, T. Huang, B.A. Gurney, V. Speriosu, Appl. Phys. Lett. 64 (20) (1994) 2736.
- [22] M. Shima, L. Salamanca-Riba, T.P. Moffat, R.D. McMichael, L.J. Swartzendruber, J. Appl. Phys. 84 (3) (1998) 1504.
- [23] C.H. Lee, H. He, F.J. Lamelas, W. Vavra, C. Uher, R. Clarke, Phys. Rev. B 42 (1) (1990) 1066.
- [24] M. J. Donahue, D. G. Porter, OOMMF User's Guide, Version 1.0, Interagency Report NISTIR 6376, NIST, Gaithersburg, MD (September 1999). <http://math.nist.gov/ommf>.
- [25] J.-G. Zhu, in: M. De Graef, Y. Zhu (Eds.), Magnetic Imaging and its Applications to Materials, Academic Press, London, UK, 2001 pp. 9.
- [26] D. Pescia, G. Zampieri, M. Stampanoni, G.L. Bona, R.F. Willis, F. Meier, Phys. Rev. Lett. 58 (9) (1987) 933.
- [27] J. Shi, J. Li, S. Tehrani, J. App. Phys. 91 (10) (2002) 7458.
- [28] M. Schneider, H. Hoffman, J. Zweck, J. Magn. Magn. Matter. 257 (2003) 1.
- [29] M. Schneider, H. Hoffman, J. Zweck, Appl. Phys. Lett. 79 (19) (2001) 3113.
- [30] S. Felton, K. Gunnarsson, P.E. Roy, P. Svedlindh, A. Quist, J. Magn. Magn. Matter. 280 (2–3) (2002) 202.
- [31] M. Lohndorf, A. Wadas, H.A.M. van den Berg, R. Wiesendanger, Appl. Phys. Lett. 68 (25) (1996) 3635.
- [32] R. Pulwey, M. Zolfl, G. Bayreuther, D. Weiss, J. Appl. Phys. 91 (10) (2002) 7995.
- [33] B.D. Cullity, Introduction to Magnetic Materials, Pearson Addison Wesley, Boston, MA, 1972, pp. 614.
- [34] M. Natali, I.L. Prejbeanu, A. Lebib, L.D. Buda, K. Ounadjela, Y. Chen, Phys. rev. lett. 88 (2002) 157203.
- [35] E.C. Stoner, E.P. Wohlfarth, Philos. Trans. Roy. Soc. A- 240 (1948) 599.
- [36] J.A. Osborn, Phys. Rev. 67 (11–12) (1945) 351.
- [37] R.D. McMichael, J. Eicke, M.J. Donahue, D.G. Porter, J. Appl. Phys. 87 (9) (2000) 7058.
- [38] R.D. McMichael, M.J. Donahue, IEEE Trans. Magn. 33 (1997) 4167.
- [39] K. Ounadjela, I.L. Prejbeanu, L.D. Buda, U. Ebels, M. Hehn, in: M. Zeise, M.J. Thornton (Eds.), Spin Electronics, Springer, Heidelberg, Germany, 2001 pp. 352.
- [40] R.D. Gomez, in: M. De Graef, Y. Zhu (Eds.), Magnetic Imaging and its Applications to Materials, Academic Press, London, UK, 2001 pp. 84.
- [41] A. Carl, J. Lohan, S. Kirsch, E.F. Wassermann, J. Appl. Phys. 89 (11) (2001) 6098.
- [42] S. McVittie, R.P. Ferrier, J. Scott, G.S. White, A. Gallagher, J. Appl. Phys. 89 (7) (2001) 3656.
- [43] D.G. Streblechenko, M.R. Scheinfein, M. Mankos, K. Babcock, IEEE Trans. Magn. 32 (5) (1996) 4124.